A&A 578, A124 (2015)
DOI: 10.1051/0004-6361/201424220


Astronomy & Astrophysics

# $C_2H$ observations toward the Orion Bar⋆

Z. Nagy[1,2], V. Ossenkopf[1], F. F. S. Van der Tak[3,4], A. Faure[5], Z. Makai[1], and E. A. Bergin[6]

[1] I. Physikalisches Institut, Universität zu Köln, Zülpicher Str. 77, 50937 Köln, Germany
e-mail: zsofia.nagy.astro@gmail.com
[2] Department of Physics and Astronomy, University of Toledo, 2801 West Bancroft Street, Toledo, OH 43606, USA
[3] Kapteyn Astronomical Institute, University of Groningen, PO box 800, 9700 AV Groningen, The Netherlands
[4] SRON Netherlands Institute for Space Research, Landleven 12, 9747 AD Groningen, The Netherlands
[5] Université Joseph Fourier/CNRS, Institut de Planétologie et d'Astrophysique de Grenoble (IPAG) UMR 5274, 38041 Grenoble, France
[6] University of Michigan, Ann Arbor, MI 48197, USA

Received 15 May 2014 / Accepted 20 April 2015

**ABSTRACT**

*Context.* The ethynyl radical ($C_2H$) is one of the first radicals to be detected in the interstellar medium. Its higher rotational transitions have recently become available with the *Herschel* Space Observatory.
*Aims.* We aim to constrain the physical parameters of the $C_2H$ emitting gas toward the Orion Bar.
*Methods.* We analyze the $C_2H$ line intensities measured toward the Orion Bar $CO^+$ Peak and *Herschel*/HIFI maps of $C_2H$, CH, and $HCO^+$ and a NANTEN map of [CI]. We interpret the observed $C_2H$ emission using the combination of *Herschel*/HIFI and NANTEN data with radiative transfer and PDR models.
*Results.* Five rotational transitions of $C_2H$ (from $N = 6–5$ up to $N = 10–9$) have been detected in the HIFI frequency range toward the $CO^+$ peak of the Orion Bar. Based on the five detected $C_2H$ transitions, a single component rotational diagram analysis gives a rotation temperature of ∼64 K and a beam-averaged $C_2H$ column density of $4 \times 10^{13}$ cm$^{-2}$. The rotational diagram is also consistent with a two-component fit, resulting in rotation temperatures of 43 ± 0.2 K and 123 ± 21 K and in beam-averaged column densities of $\sim 8.3 \times 10^{13}$ cm$^{-2}$ and $\sim 2.3 \times 10^{13}$ cm$^{-2}$ for the three lower-$N$ and for the three higher-$N$ transitions, respectively. The measured five rotational transitions cannot be explained by any single parameter model. According to a non-LTE model, most of the $C_2H$ column density produces the lower−$N$ $C_2H$ transitions and traces a warm ($T_{kin} \sim 100–150$ K) and dense ($n(H_2) \sim 10^5–10^6$ cm$^{-3}$) gas. A small fraction of the $C_2H$ column density is required to reproduce the intensity of the highest-$N$ transitions ($N = 9–8$ and $N = 10–9$) originating in a high-density ($n(H_2) \sim 5 \times 10^6$ cm$^{-3}$) hot ($T_{kin} \sim 400$ K) gas. The total beam-averaged $C_2H$ column density in the model is $10^{14}$ cm$^{-2}$. A comparison of the spatial distribution of $C_2H$ to those of CH, $HCO^+$, and [CI] shows the best correlation with CH.
*Conclusions.* Both the non-LTE radiative transfer model and a simple PDR model representing the Orion Bar with a plane-parallel slab of gas and dust suggest that $C_2H$ cannot be described by a single pressure component, unlike the reactive ion $CH^+$, which was previously analyzed toward the Orion Bar $CO^+$ peak. The physical parameters traced by the higher rotational transitions ($N = 6–5$, ..., $10–9$) of $C_2H$ may be consistent with the edges of dense clumps exposed to UV radiation near the ionization front of the Orion Bar.

**Key words.** stars: formation – ISM: molecules

## 1. Introduction

The ethynyl radical ($C_2H$) was one of the first radicals to be detected in the interstellar medium (Tucker et al. 1974). It has been observed toward several types of regions, including diffuse clouds (Lucas & Liszt 2000), massive star-forming regions (Beuther et al. 2008), photon-dominated regions (PDRs, e.g. Teyssier et al. 2004) and dark clouds (e.g., Pratap et al. 1997). $C_2H$ is an important molecule in the carbon-chemistry and is related to many C-bearing species. One example is the $C_3H^+$ ion, which has recently been detected toward the Horsehead PDR (Pety et al. 2012). $C_2H$ can also be an ingredient for the formation of carbon chain molecules, such as $C_5$, via a reaction with $C_3$. $C_2H$ can also be converted to CO either by a neutral-neutral reaction with O or by a reaction with carbon chain ions, such as $HCO^+$. Its role in the carbon chemistry means that understanding the abundance of $C_2H$ is important to understanding the chemical network related to carbon. The recent access to the higher rotational transitions provided by the *Herschel* Space Observatory and the recently calculated inelastic collision rates (Spielfiedel et al. 2012) give an opportunity to probe the chemistry and excitation of $C_2H$. Using the higher rotational transitions accessible by *Herschel* and the available collision rates we probe the excitation of $C_2H$ and the physical parameters that it traces toward the prototypical, high UV-illumination PDR, the Orion Bar. As photodissociation of larger carbon-chain molecules and polycyclic aromatic hydrocarbons (PAHs) is one of the possible formation routes of $C_2H$, PDRs provide a good source to study $C_2H$.

The Orion Bar is an ideal source for probing the excitation and chemistry of molecules in PDRs, thanks to its close distance of 414 pc (Menten et al. 2007) and its well-known structure and geometry. The Orion Bar is located between the Orion molecular cloud and an HII region illuminated by the Trapezium cluster. The FUV radiation field of the Trapezium cluster at the location

⋆ Appendices are available in electronic form at http://www.aanda.org

of the Orion Bar is equivalent to $(1-4)\times10^4\chi_0$ in Draine (1978) units. Its orientation changes from face-on to nearly edge-on where the molecular emissions peak. The observations presented in this paper also correspond to the nearly edge-on orientation part of the Orion Bar. The geometrical enhancement of the column densities toward the nearly edge-on part of the Orion Bar was derived by multiple studies and is in the range between 4 and 20. The tilt angle compared to a completely edge-on orientation was suggested to be 3° in the model of Hogerheijde et al. (1995) and Jansen et al. (1995). A tilt angle of 3° is equivalent to an enhancement factor of 20 for the measured column densities. Based on OI 1.317 $\mu$m emission, Walmsley et al. (2000) find a model that requires a geometrical enhancement factor of 5 to convert the observed column densities into face-on values. Neufeld et al. (2006) find the geometrical enhancement factor to be 4 based on measured $C^+$ column densities. Using a clumpy 3D PDR model, Andree-Labsch et al. (2014) successfully reproduced the Orion Bar stratification using a clumpy edge-on cavity wall, and they claim that a model of a convex filament fails to describe the structure of the Orion Bar. The average kinetic temperature was estimated to be 85 K (Hogerheijde et al. 1995). Closer to the ionization front, higher temperatures are also measured; for example, OH transitions observed with *Herschel*/PACS are consistent with 160–220 K gas (Goicoechea et al. 2011) and $CH^+$ observations with temperatures around 500 K (Nagy et al. 2013). Part of the molecular line emission measured toward the Orion Bar corresponds to an "interclump medium" with densities between a few $10^4$ and $2\times10^5$ cm$^{-3}$ (Simon et al. 1997). It has been suggested that other molecular lines originate in clumps with densities in the range between $1.5\times10^6$ and $6\times10^6$ cm$^{-3}$ (Lis & Schilke 2003).

Previous $C_2H$ observations toward the Orion Bar cover the lower-$N$ rotational transitions. Cuadrado et al. (2015) analyze the $N$ = 1–0, ..., 4–3 transitions. The $N$ = 4–3 transition was observed by Hogerheijde et al. (1995), Jansen et al. (1995), and Van der Wiel et al. (2009)), and the $N$ = 1–0 transition by Fuente et al. (1996). In this paper we analyze emission from five higher rotational transitions to constrain the physical parameters of the $C_2H$ emitting gas toward the Orion Bar.

## 2. Observations and data reduction

The observations presented in this paper are part of the HEXOS[1] guaranteed-time key program (Bergin et al. 2010) for the HIFI instrument (De Graauw et al. 2010) of the *Herschel* Space Observatory (Pilbratt et al. 2010). The $CO^+$ peak ($\alpha_{J2000}$ = $05^h35^m20.6^s$, $\delta_{J2000}$ = −05°25′14″) of the Orion Bar has been observed over the full HIFI range (480-1910 GHz) as a spectral scan. An overview of the full spectral line survey will be presented in a forthcoming paper (Nagy et al. 2015). The data were reduced using HIPE (Ott 2010) pipeline version 9.0 and 10.0 and are calibrated to $T_A^\star$ scale. The sideband deconvolution was done using the *doDeconvolution* task in HIPE. The double sideband (DSB) scans were first deconvolved with the strongest lines ($T_A^*$ > 10 K) removed. This deconvolution results in a single sideband (SSB) spectrum with very little contribution from deconvolution ghosts, but without data at the frequencies of the strongest lines. Therefore, we performed another deconvolution of the data including the strongest lines. The data around the frequencies of the strong lines was then used with the first deconvolution result, providing a single sideband spectrum in the total observed frequency range.

[1] *Herschel* observations of EXtra-Ordinary Sources.

The continuum at the observed frequencies is negligible, because it is similar to the measured rms noise level. The $C_2H$ transitions detected in the HIFI survey are listed in Table 1 and include spectroscopic parameters from the Cologne Database for Molecular Spectroscopy (CDMS, Müller et al. 2005). The hyperfine structure is not resolved by HIFI, therefore the detected lines are blends of multiple hyperfine components. Table 1 lists the spectroscopic parameters for the strongest hyperfine components. The spectral resolutions at the frequencies of the observed transitions (from $N$ = 6–5 to $N$ = 10–9) are 0.29, 0.25, 0.21, 0.19, and 0.17 km s$^{-1}$.

To compare the line intensities of the transitions detected with different beam sizes in the HIFI line survey, we converted all the observed line intensities to a common ~40.5″ resolution. We derived conversion factors between the original beam sizes and ~40.5″ based on the integrated intensity map of the $C_2H$ 4–3 transition from the *James Clerk Maxwell* Telescope (JCMT) Spectral Legacy Survey (Van der Wiel et al. 2009). The derived correction factors between the beam sizes of the $C_2H$ transitions and the 40.5″ beam are 0.94, 0.88, 0.84, and 0.79 from beam sizes of 34.7″, 30.4″, 27.0″, and 24.3″ , respectively. Table 1 includes the parameters that are measured with the original beam sizes. For the non-local thermodynamic equilibrium (non-LTE) models in Sect. 5, we used the values that have been corrected for the changing beam size.

In addition to the HIFI spectral scans, a 115″×65″ area centered on $\alpha_{J2000}$ = $05^h35^m20.81^s$, $\delta_{J2000}$ = −05°25′17.1″ with a position angle of 145° was mapped in the $N$ = 6–5 transition of $C_2H$ with HIFI, in on-the-fly (OTF) mapping mode with position-switch reference. The center of the maps is consistent with the $CO^+$ peak (it is 4″ off from the $CO^+$ peak) where the spectral scans are pointed. The $CO^+$ peak is close to the PDR surface and to the region where vibrationally excited $H_2$ peaks (e.g., Walmsley et al. 2000 and Fig. 1. of Nagy et al. 2013). The fully sampled map was pipelined with HIPE 11.1 and exported to CLASS for further analysis, including baseline subtraction using linear baselines. As a comparison to the $C_2H$ emission, we used maps of the $HCO^+$ $J$ = 6–5 transition (535 061.6 MHz) and of the CH $^2\Pi_{3/2}$ transitions around 536 GHz ($N$ = 1–0, $J$ = 3/2–1/2, $F$ = $2^-$–$1^+$ at 536.76115 MHz, $N$ = 1–0, $J$ = 3/2–1/2, $F$ = $1^-$ – $1^+$ at 536782.0 MHz, $N$ = 1–0, $J$ = 3/2–1/2, $F$ = $1^-$–$0^+$ at 536.79568). These maps have the same parameters and were reduced with the same HIPE version and methods as the $C_2H$ $N$ = 6–5 map. The spectral resolution of the observed $HCO^+$ and CH transitions is 0.28 km s$^{-1}$.

In addition to the HIFI maps, we used a [CI] $^3P_1$–$^3P_0$ (492.1607 GHz) map observed with the NANTEN2-4 m antenna, which is located at 4865 m altitude in Pampa la Bola in northern Chile. The observations were taken in October and November 2011 with a dual-channel 460/810 GHz SMART receiver. The receiver temperature was ~250 K at the band center. The velocity resolution (or channel spacing) is 0.68 km s$^{-1}$ at 460 GHz. The observed spectra were calibrated using the atmospheric model atmospheric transmision at microwave (Pardo et al. 2001). The half power beam width (HPBW) is ~37″. The data were calibrated to main beam temperature using main beam and forward efficiencies of 0.50 and 0.86, respectively.

## 3. The spatial distribution and velocity structure of $C_2H$

Figure 1 shows the integrated intensity of the $C_2H$ $N$ = 6–5 $J$ = 13/2–11/2 and $J$ = 11/2–9/2 doublet. $C_2H$ emission has

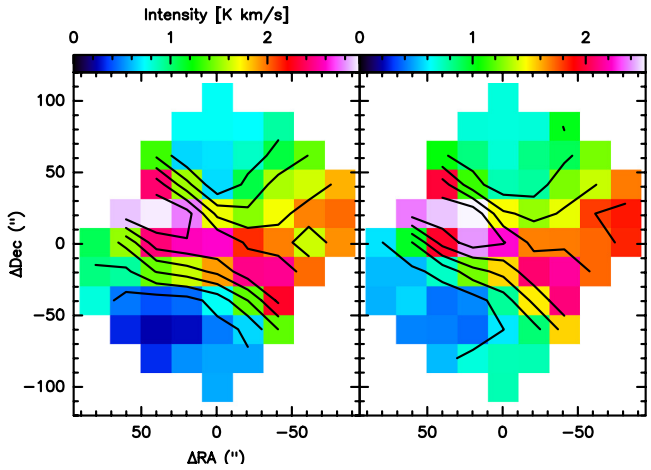


**Fig. 1.** Integrated intensities of the $C_2H$ $N = 6–5$ $J = 13/2–11/2$ (*left*) and $J = 11/2–9/2$ (*right*) doublet. The contour levels go from 0.2 to 2.8 K km s$^{-1}$spaced by 0.4 K km s$^{-1}$.

been detected toward the Bar and also perpendicular to the Bar, corresponding to the Orion Ridge. The $C_2H$ $N = 6–5$ emission is not as extended as other species, including CH and [CI] (Fig. 4). The $C_2H$ integrated intensity does not peak at the $CO^+$ peak (the center of the maps), but toward the northeastern part of the Bar covered by the $C_2H$ map around offsets (45″, 25″). The difference in the position where the $C_2H$ and $CO^+$ line intensities peak is likely to be a result of different physical parameters toward the two positions. As mentioned in Sect. 7, $C_2H$ formation for the Orion Bar is expected to be dominated by a reaction of $C_2$ with $H_2$. $CO^+$ is produced in a reaction between $C^+$ and OH, where OH is produced from O and $H_2$. Therefore, the $CO^+$ and $C_2H$ peaks likely have different $H_2$ volume densities. The region where $C_2H$ peaks overlaps with one of the $OH^+$ intensity peaks (at a velocity of ∼12 km s$^{-1}$, Van der Tak et al. 2013), which lies about 10″ southeast of the CO 10-9 intensity peak at a velocity of ∼12 km s$^{-1}$, which is observed toward the $H^{13}CN$ clumps 2 and 3 identified by Lis & Schilke (2003).

Apart from the $N = 6–5$ doublet, four more doublets (from $N = 7–6$ to $N = 10–9$) have been detected toward the $CO^+$ peak of the Orion Bar, which the $N = 6–5$ map is centered on. Figure 2 shows the line profiles of the $C_2H$ doublets observed there. The observed two lines, which are blends of hyperfine transitions, are shifted with ∼62 MHz in every case, which is equivalent to different velocity intervals due to the change in the frequency of the transitions. Table 1 lists the line intensities of these $C_2H$ transitions as obtained by Gaussian fitting. The observed doublet intensity ratios are 1.23, 1.16, 1.07, 1.26, and 0.66 for $N = 6–5, ..., 10–9$, respectively. In LTE, the doublet ratio is given by the ratio of the A coefficients so that we expect that the blueshifted component is about 2% brighter than the red one. The opposite ratio in $N = 10–9$ is probably due to the lower S/N, leading to an overestimate of the width and integrated intensity in the redshifted component. The peak velocities are in the range between 10.6–11.1 km s$^{-1}$. The variation in the peak velocities falls slightly above the uncertainty from the frequency accuracy of the HIFI products and the fit accuracy so that it may indicate a small velocity variation within the $C_2H$ emitting gas, but it is very small compared to the line width, so that we can ignore it here, but still make certain that we analyze the same gas in all transitions. As shown in Fig. 3 on the velocity channel maps of $C_2H$, the Orion Ridge is most prominent at velocities lower than 9 km s$^{-1}$. Most $C_2H$ emission toward the Orion Bar is seen

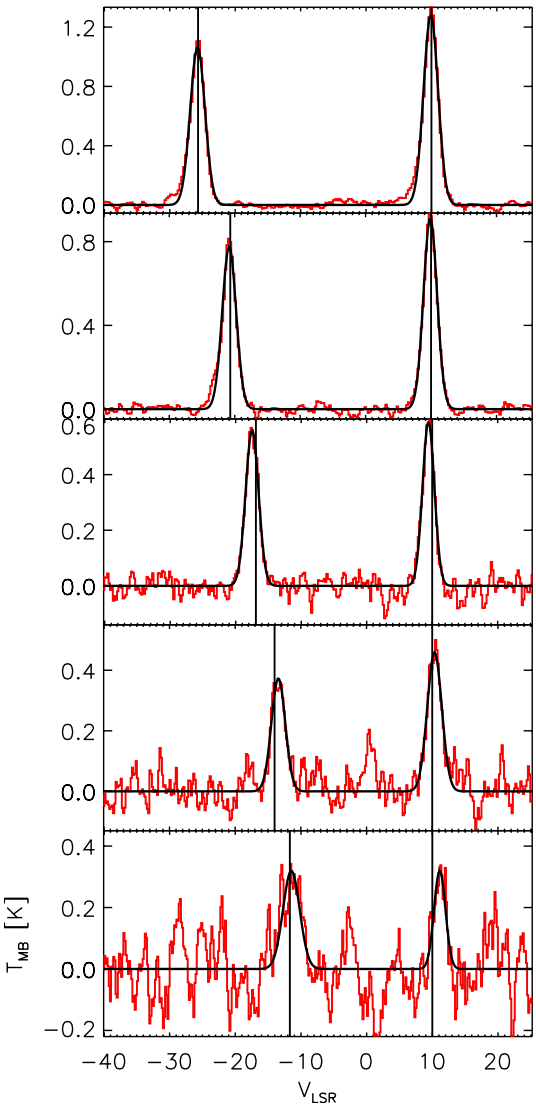


**Fig. 2.** Line profiles of the $C_2H$ doublets observed toward the $CO^+$ peak of the Orion Bar from $N = 6–5$ (*top*) to $N = 10–9$ (*bottom*). The Gaussian fits shown in Table 1 are overlaid on the profiles. The black lines show the expected LSR velocity of 10 km s$^{-1}$for both components.

at velocities in the range between 9 and 11 km s$^{-1}$. The velocity structure of $C_2H$ is similar to that seen in $OH^+$ (Van der Tak et al. 2013): the blueshifted part of the emission peaks toward the Orion Ridge, emission around the expected source velocity (10 km s$^{-1}$) has contributions both from the Orion Bar and the Orion Ridge, while emission corresponding to the redshifted velocities only comes from the Bar. However, the peak velocities at which the Orion Bar and Ridge are detected are slightly shifted for $C_2H$ compared to those for $OH^+$. $OH^+$ at velocities of 9–10 km s$^{-1}$shows emission mainly toward the Orion Ridge. In the same velocity interval, $C_2H$ emission peaks toward the Orion Bar and shows little emission toward the Orion Ridge. This could be explained by low-density gas in the Orion Ridge at $v < 9$ km s$^{-1}$ providing a lower $C_2H$ excitation compared to $OH^+$ for that component.

Figure 4 shows the spatial distribution of $C_2H$ $N = 6–5$ and lines of other species that are expected to trace regions relatively close to the PDR surface (equivalent to low visual extinctions): CH $^2\Pi_{3/2}$ $N = 1–0$ $J = 3/2–1/2$, $HCO^+$ $J = 6–5$, and [CI] $^3P_1–^3P_0$. Out of the four line emissions shown in Fig. 4, the

**Table 1.** Spectroscopic and Gaussian-fit parameters of the $C_2H$ lines observed toward the $CO^+$ peak of the Orion Bar.

| Transition | $A_{ij}$ ($s^{-1}$) | $E_u$ (K) | $\nu$ (MHz) | $\int T_{MB}dV$ (K km $s^{-1}$) | $V_{LSR}$ (km $s^{-1}$) | $\Delta V$ (km $s^{-1}$) | $T_{peak}$ (K) | rms (K) | $\Theta_B$ ($''$) |
|---|---|---|---|---|---|---|---|---|---|
| $N$ = 6–5, $J$ = 13/2–11/2 | $4.54 \times 10^{-4}$ | 88.0 | 523 971.6 | 3.64 ± 0.03 | 10.59 ± 0.08 | 2.65 ± 0.03 | 1.29 | 0.02 | 40.5 |
| $N$ = 6–5, $J$ = 11/2–9/2 | $4.46 \times 10^{-4}$ | 88.0 | 524 033.9 | 2.95 ± 0.03 | 10.58 ± 0.01 | 2.61 ± 0.03 | 1.06 | 0.02 | 40.5 |
| $N$ = 7–6, $J$ = 15/2–13/2 | $7.30 \times 10^{-4}$ | 117.4 | 611 267.2 | 2.38 ± 0.16 | 10.77 ± 0.07 | 2.44 ± 0.19 | 0.91 | 0.13 | 34.7 |
| $N$ = 7–6, $J$ = 13/2–11/2 | $7.21 \times 10^{-4}$ | 117.4 | 611 329.7 | 2.06 ± 0.14 | 10.70 ± 0.03 | 2.50 ± 0.20 | 0.78 | 0.11 | 34.7 |
| $N$ = 8–7, $J$ = 19/2–17/2 | $1.10 \times 10^{-3}$ | 150.9 | 698 544.8 | 1.32 ± 0.09 | 10.67 ± 0.07 | 2.12 ± 0.17 | 0.59 | 0.09 | 30.4 |
| $N$ = 8–7, $J$ = 17/2–15/2 | $1.09 \times 10^{-3}$ | 150.9 | 698 607.5 | 1.23 ± 0.10 | 10.67 ± 0.08 | 2.23 ± 0.21 | 0.52 | 0.10 | 30.4 |
| $N$ = 9–8, $J$ = 19/2–17/2 | $1.58 \times 10^{-3}$ | 188.6 | 785 802.1 | 1.21 ± 0.09 | 10.35 ± 0.09 | 2.51 ± 0.23 | 0.45 | 0.08 | 27.0 |
| $N$ = 9–8, $J$ = 17/2–15/2 | $1.57 \times 10^{-3}$ | 188.6 | 785 865.0 | 0.96 ± 0.10 | 10.56 ± 0.12 | 2.44 ± 0.28 | 0.37 | 0.09 | 27.0 |
| $N$ = 10–9, $J$ = 21/2–19/2 | $2.18 \times 10^{-3}$ | 230.5 | 873 036.4 | 0.82 ± 0.10 | 11.12 ± 0.15 | 2.23 ± 0.30 | 0.35 | 0.11 | 24.3 |
| $N$ = 10–9, $J$ = 19/2–17/2 | $2.16 \times 10^{-3}$ | 230.5 | 873 099.5 | 1.25 ± 0.11 | 10.11 ± 0.18 | 3.00 ± 0.50 | 0.30 | 0.09 | 24.3 |

lines of CH and [CI] show the largest spatial extent over the area analyzed in this paper. All these lines peak at a similar position toward the Orion Bar. $HCO^+$ $J$ = 6–5 emission toward the Orion Bar is less extended compared to the lines of the other molecules, especially [CI] and CH. $HCO^+$ $J$ = 6–5 is also the only line in Fig. 4 that peaks toward the Orion Ridge and not toward the Bar. The comparison of the spatial distribution of $C_2H$ to those of $HCO^+$, CH, and [CI] based on the line emissions shown in Fig. 4 is straightforward, due to the similar beam size of the observed transitions. In the following paragraphs while comparing the spatial distribution of $C_2H$ to those of CH, $HCO^+$, and [CI], we refer to the transitions shown in Fig. 4. The spatial distribution of the species may vary depending on the transitions used. The comparison of the spatial distributions can be converted to correlation plots (Fig. 5). $C_2H$ shows the strongest correlation with CH, compared to $HCO^+$ and [CI]. The corresponding correlation coefficients for CH, $HCO^+$, and [CI] are 0.93, 0.81, and 0.68, respectively.

As seen in the velocity channel maps, the velocity range covered by the observed lines corresponds to at least two regions: the Orion Bar and the Orion Ridge. They represent two different PDRs with different conditions so that we expect a different behavior. Therefore, the spatial correlation may be different for the spatially different regions. Figure 6 shows spatial correlations between $C_2H$, CH, $HCO^+$, and [CI] calculated in three velocity intervals: 7–8.5 km $s^{-1}$, 8.5–10 km $s^{-1}$, and 10–11.5 km $s^{-1}$. The blueshifted velocity interval is dominated by emission from the Orion Ridge. The central velocity interval has contributions both from the Orion Bar and the Orion Ridge. The redshifted velocity interval is dominated by emission from the Orion Bar. The best correlation is found for the blueshifted (correlation coefficients of 0.69–0.92), and the worst for the intermediate velocity intervals (correlation coefficients of 0.38–0.68). The decrease in the correlation coefficient for the central velocity interval may be related to optical depth effects. Based on these results, CH and $HCO^+$ may be good tracers of $C_2H$ for the Orion Ridge. Taking only the redshifted velocity interval into account, these species may probe a similar gas to $C_2H$. Among the molecules studied here, the gas traced by [CI] is the least related to the gas traced by $C_2H$ both for the Bar and the Ridge.

## 4. $C_2H$ column densities – single excitation temperature

One method of estimating the $C_2H$ column density is to interpret the intensities of the observed five doublets by a rotational diagram. The observed integrated intensities can be directly converted to upper state column densities by assuming that the transitions are optically thin, that the level populations can be characterized by a single excitation temperature, and that the line emission has a uniform beam filling. In the rotational diagram method, the measured integrated main-beam temperatures of lines ($\int T_{MB}dV$ K km $s^{-1}$) are converted to the column densities of the molecules in the upper level ($N_u$) using

$$\frac{N_u}{g_u} = \frac{N_{tot}}{Q(T_{rot})} \exp\left(-\frac{E_u}{T_{rot}}\right) = \frac{1.67 \times 10^{14}}{\nu \mu^2 S} \int T_{MB} dV, \quad (1)$$

with $g_u$ the statistical weight of level u, $N_{tot}$ the total column density in $cm^{-2}$, $Q(T_{rot})$ the partition function for $T_{rot}$, $E_u$ the upper level energy in K, $\nu$ the frequency in GHz, $\mu$ the permanent dipole moment in Debye, and $S$ the line strength value. A linear fit to $\ln(N_u/g_u)-E_u$ gives $T_{rot}$ as the inverse of the slope, and $N_{tot}$, the column density as the intercept. The rotational temperature would be expected to be equal to the kinetic temperature if all levels were thermalized.

Figure 7 shows the resulting rotation diagram when adding the hyperfine components of each rotational transition, which corresponds to a rotation temperature of ~64 ± 11 K and a $C_2H$ column density of $(4 \pm 0.7) \times 10^{13}$ $cm^{-2}$. The ratios of the intensities of the hyperfine components are consistent with the optically thin assumption.

The curved rotational diagram in Fig. 7 may be proof that multiple density and temperature components are present in the region covered by the HIFI beam. We therefore fitted the $N$ = 6–5, ..., 8–7 and the $N$ = 8–7, ..., 10–9 transitions separately as well. The rotation diagram of the lower-$N$ transitions gives a rotation temperature of 43 ± 0.2 K and a column density of $(8 \pm 0.03) \times 10^{13}$ $cm^{-2}$. The rotation diagram fit for the higher-$N$ transitions gives a rotation temperature of ~123 ± 21 K and a column density of $(2 \pm 0.4) \times 10^{13}$ $cm^{-2}$. For the two-component rotational diagram, the total beam-averaged $C_2H$ column density is $10^{14}$ $cm^{-2}$. This is similar to the maximum value that Jansen et al. (1995) found along their observed cut toward the Orion Bar, and to the factors of 2–5 below the values that Van der Wiel et al. (2009) derived, both corresponding to beam sizes of ~15″.

## 5. $C_2H$ column densities – non-LTE calculation

Since inelastic collision rates for $C_2H$ have recently become available, a non-LTE analysis is also possible. Non-LTE excitation is expected to be important because the transitions studied here have critical densities above the average ~$10^5$ $cm^{-3}$ Orion Bar $H_2$ volume density (Hogerheijde et al. 1995). For example, when assuming a gas temperature of 100 K, the $N$ = 6–5, $J$ = 13/2–11/2 transition for $C_2H$-$H_2$ collisions has a critical

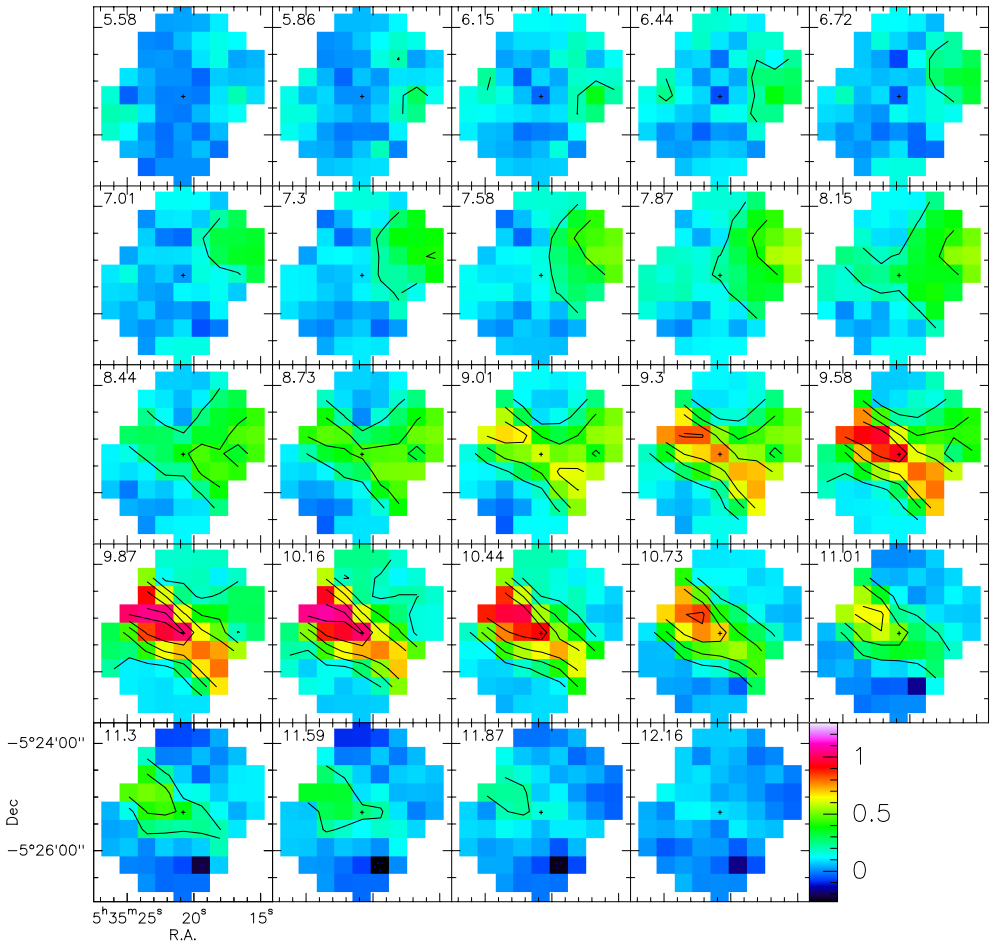


**Fig. 3.** Velocity channel maps of the $C_2H$ $N = 6–5$ $J = 13/2–11/2$ transition toward the Orion Bar.

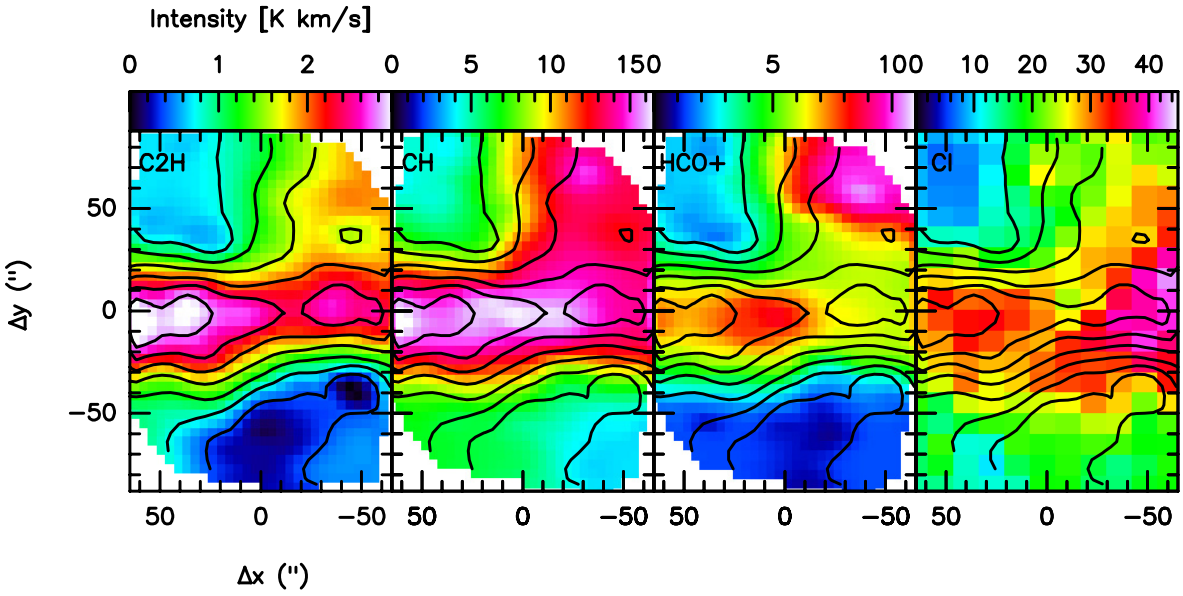


**Fig. 4.** Integrated intensity maps of $C_2H$ $N = 6–5$, CH $^2\Pi_{3/2}$, $HCO^+$ $J = 6–5$, and [CI] $^3P_1–^3P_0$ toward the Orion Bar. The $C_2H$ integrated intensities are overplotted on each map (black contours). The maps have been rotated by −35°.

density of $6.8 \times 10^7$ cm$^{-3}$, and the $N = 8–7$, $J = 17/2–15/2$ a critical density of $1.6 \times 10^8$ cm$^{-3}$. While the LTE approach provides information on the $C_2H$ column density and excitation temperature, the non-LTE analysis also gives an estimate of the kinetic temperature and $H_2$ volume density of the $C_2H$ emitting gas. This is, of course, only possible if the excitation deviates from LTE, but this is expected at least for the high-$N$ transitions with very high critical densities. $C_2H$-He collision rates were calculated by Spielfiedel et al. (2012), which we scaled to represent $C_2H$-$H_2$ collisions following Schöier et al. (2005) by a

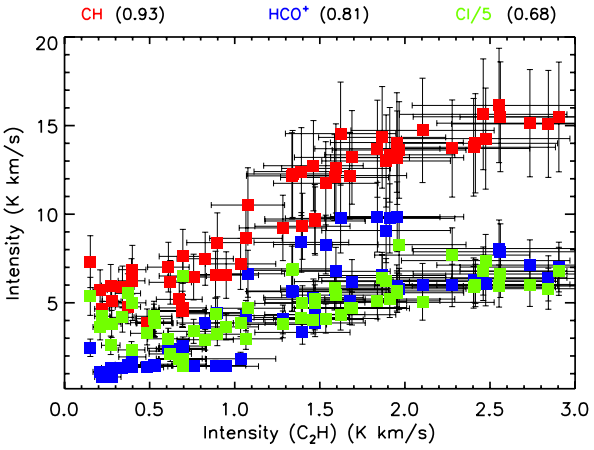


**Fig. 5.** Integrated line intensity correlations between the $C_2H$ $N = 6–5$ $J = 13/2–11/2$ line and $HCO^+$, CH, and [CI]. The corresponding correlation coefficients are shown in parentheses.

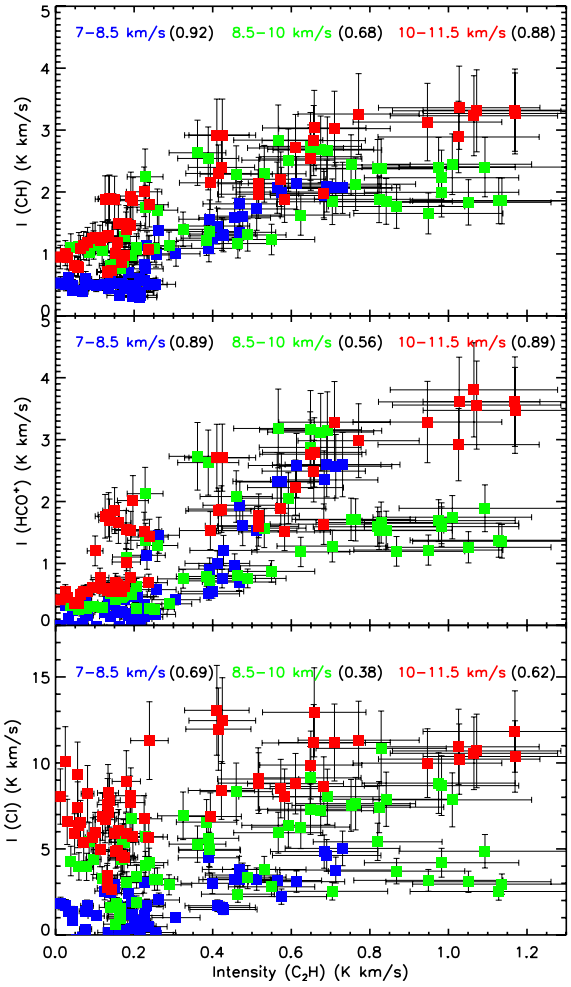


**Fig. 6.** Line intensity spatial correlations between the $C_2H$ $N = 6–5$ $J = 13/2–11/2$ line and $HCO^+$, CH, and [CI]. The corresponding correlation coefficients are shown in parentheses.

factor of 1.36, based on the ratio of the reduced mass of the $C_2H$-He and $C_2H$-$H_2$ systems. These collision rates are available for energies up to 104.9 $cm^{-1}$, covering three rotational transitions analyzed in this paper ($N = 6–5$, 7–6, and 8–7). The rates were calculated for a temperature range between 5 K and 100 K. We extrapolated these collision rates for temperatures up to 400 K

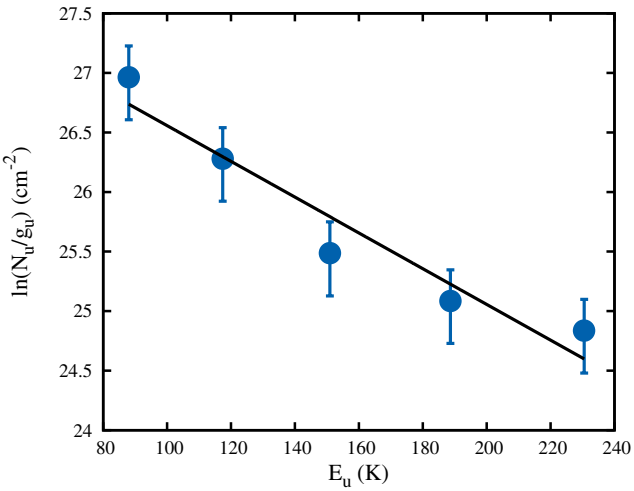


**Fig. 7.** Rotational diagram of $C_2H$, corresponding to a rotational temperature of 64 ± 11 K and a column density of $(4 \pm 0.02) \times 10^{13}$ $cm^{-2}$.

and energies up to ~445 $cm^{-1}$ (see Appendix B). Collisional rates for these higher levels and temperatures are clearly required and should be computed properly to avoid extrapolations. We also used collision rates with electrons, calculated in the Born approximation with infinite-order-sudden (IOS) recoupling, calculated for temperatures in the range between 10 K and 1000 K (see Appendix A). We ran several RADEX (Van der Tak et al. 2007) models with physical parameters that are expected for the Orion Bar, i.e., kinetic temperatures between 50 and 400 K and $H_2$ volume densities between $5 \times 10^4$ $cm^{-3}$ and $10^7$ $cm^{-3}$. We also used a background radiation field based on Arab et al. (2012), which is a modified blackbody distribution with a dust temperature of $T_d = 50$ K and a dust emissivity index of $\beta = 1.6$. The used electron density has very little effect on the line intensities, which is a consequence of the small $C_2H$ dipole moment (Appendix A).

The observed line intensities are not consistent with $C_2H$ originating in a single gas component toward the Orion Bar $CO^+$ peak. A two-component model is required to fit the observed $C_2H$ intensities. In this model the $C_2H$ column density is dominated by a gas component with a temperature of 100 K to 150 K, an $H_2$ volume density of $5 \times 10^5–10^6$ $cm^{-3}$, and a $C_2H$ column density of $8 \times 10^{13}$ $cm^{-2}$. To reproduce the integrated intensity of the highest-$N$ ($N = 9–8$ and 10–9) doublets, a higher density ($5 \times 10^6$ $cm^{-3}$), hot ($T \sim 400$ K) gas component is required. This second component has a column density of $2 \times 10^{13}$ $cm^{-2}$. The sum of the line intensities predicted by this two-component model are overplotted on the observed line intensities in Fig. 8. This model is consistent with the $N = 6–5$, 7–6, and 10–9 doublets within the observational errors, and overpredict the 8–7 and 9–8 doublets by 40% and 30%, respectively. This model is also consistent with the assumption that the analyzed $C_2H$ transitions are optically thin: the opacity of every transition is less than 0.03 in each model. The doublet ratios are reproduced well (13% or better) by both two-component models for the $N = 6–5$,..., 9–8 transitions. The doublet ratio for the $N = 10–9$ transition is reproduced within a factor of two. The doublet ratios estimated with RADEX for the two-component model with $n(H_2) = 10^6$ $cm^{-3}$, $T_{kin} = 100$ K, $n(H_2) = 5 \times 10^6$ $cm^{-3}$, and $T = 400$ K are 1.32, 1.27, 1.23, 1.22, and 1.22 for $N = 6–5$, ..., 10–9, respectively. The doublet ratios for the two component model with $n(H_2) = 5 \times 10^5$ $cm^{-3}$, $T_{kin} = 150$ K,

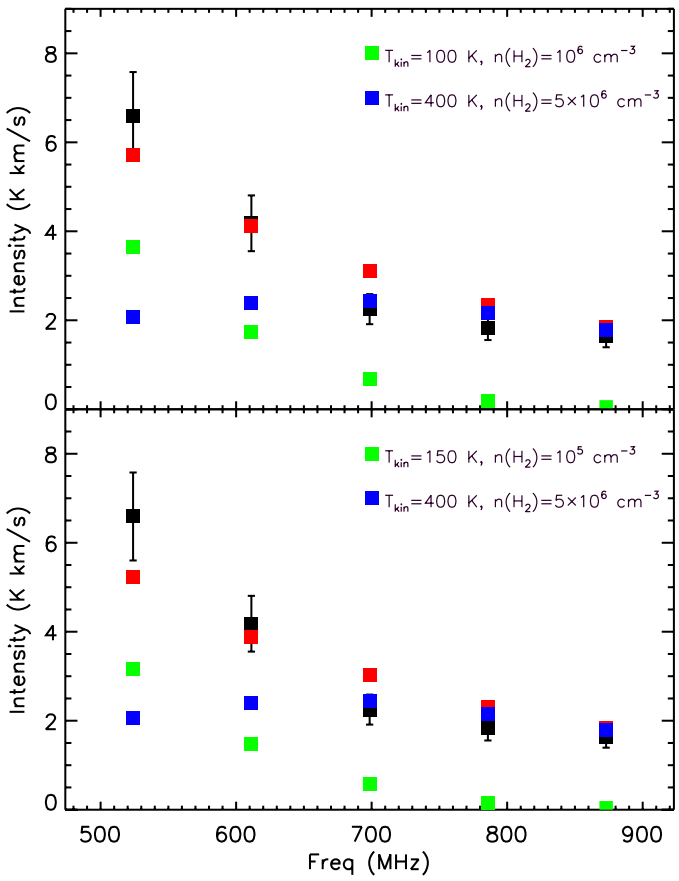


**Fig. 8.** Non-LTE $C_2H$ line intensity predictions with RADEX vs. the observed line intensities (black symbols). *Top panel*: the models correspond to parameters of $n(H_2) = 10^6$ cm$^{-3}$, $T_{kin} = 100$ K, $N(C_2H) = 8 \times 10^{13}$ cm$^{-2}$ (green symbols), and to $n(H_2) = 5 \times 10^6$ cm$^{-3}$, $T_{kin} = 400$ K, $N(C_2H) = 2 \times 10^{13}$ cm$^{-2}$ (blue symbols). The sum of the two components is given by the red symbols. *Bottom panel*: the models correspond to parameters of $n(H_2) = 10^5$ cm$^{-3}$, $T_{kin} = 150$ K, $N(C_2H) = 8 \times 10^{13}$ cm$^{-2}$ (green symbols), and to $n(H_2) = 5 \times 10^6$ cm$^{-3}$, $T_{kin} = 400$ K, $N(C_2H) = 2 \times 10^{13}$ cm$^{-2}$ (blue symbols). The sum of the two components is given by the red symbols.

$n(H_2) = 5 \times 10^6$ cm$^{-3}$ and $T = 400$ K are 1.28, 1.23, 1.20, 1.21, and 1.22.

The evidence of at least two different gas components observed toward the $CO^+$ peak is consistent with the clumpy picture of PDRs. Different density and temperature components are expected to be covered by the HIFI beam. The existence of such high-density gas toward the Orion Bar $CO^+$ peak is consistent with what was found for OH Goicoechea et al. (2011).

The non-LTE models suggest a total $C_2H$ column density of $\sim 10^{14}$ cm$^{-2}$, dominated by the lowest-$N$ transitions. The models also suggest that there is a very high-density gas component that contributes only about 20% of the $C_2H$ column density, but is required to fit the highest-$N$ transitions. The hot and dense gas that $C_2H$ traces toward the Orion Bar based on the transitions analyzed in this paper may be consistent with the UV-illuminated edges of dense clumps close to the ionization front of the PDR.

## 6. Comparison to PDR models

In earlier works based on the Orion Bar HIFI line survey, we presented an isobaric PDR model, which explained the observed $CH^+$ (Nagy et al. 2013) and $OH^+$ (Van der Tak et al. 2013) emission toward the $CO^+$ peak of the Orion Bar. This model was computed using the 1.4.4 version of the Meudon PDR code (Le Petit et al. 2006) and corresponds to a pressure of $P = 10^8$ cm$^{-3}$ K and represents a plane-parallel slab of gas and dust illuminated from two sides by a radiation field of $\chi = 10^4$ on the front and by $\chi/1000$ on the back side. We implemented the collision rates used in Sect. 5 in order to compute integrated intensities for the observed transitions.

Figure 9 shows the calculated $C_2H$ integrated intensities corresponding to the model, overplotted on the observed integrated intensities. The model overpredicts the intensity of the $N = 6-5$, $N = 7-6$, and $N = 9-8$ doublets by about factors of 2, 1.5, and 20%. The model underpredicts the intensities of the $N = 10-9$ and $N = 11-10$ doublets by factors of 2.4 and 5.5. Even though the model predictions are close to most of the observed line intensities, it is clear that assuming a single pressure component is simplification, because the structure of PDRs is clumpy. The offset between the observed and modeled values may be explained by different gas components or clumps covered by the HIFI beam. The model predicts a face-on column density of $1.7 \times 10^{14}$ cm$^{-2}$. When assuming a geometrical enhancement factor of four (e.g., Neufeld et al. 2006), this is equivalent to an edge-on column density of $6.8 \times 10^{14}$ cm$^{-2}$. This value is about a factor of 7 above the values predicted by the two-component rotational diagram and RADEX models. Despite the higher column density than in the rotational diagram and RADEX models, this model underpredicts the intensity of the highest-$N$ transitions. This confirms the result that the higher-$N$ transitions contribute only a minor part of the total $C_2H$ column density. The difference between the observed and modeled $C_2H$ intensities suggests that most $C_2H$ originates in a different gas component than $CH^+$, which was used to constrain the PDR model.

Figure 10 shows the abundances of $C_2H$, CH, $C^+$, $HCO^+$, [CI], and $CH^+$ that correspond to the model, as a function of visual extinction up to a visual extinction of 10. Most $C_2H$ is located near the surface of the PDR in a relatively narrow region at visual extinctions of $A_V \sim 1-2$. The gas temperature in this region predicted by the PDR model is in the range between ~570 K and 140 K, while the $H_2$ volume densities are in the range of $10^5$ cm$^{-3}$ and $6 \times 10^5$ cm$^{-3}$, as shown in Fig. 11. In the range of $A_V = 0.8 \ldots 1.5$ responsible for the main $C_2H$ emission, the PDR model predicts temperatures that cover both the components suggested by the RADEX models, 100−150 K and 400 K. The $H_2$ volume densities suggested by the RADEX model for the lower-$N$ transitions ($10^5-10^6$ cm$^{-3}$) is close to those corresponding to the PDR model. There are, however, two discrepancies: the RADEX $H_2$ volume density of $5 \times 10^6$ cm$^{-3}$ for the hot component is above the density range predicted by the model for the $C_2H$ emitting gas. Moreover, the temperature-density structure calculated in the isobaric model would predict the highest temperature gas to trace the lowest $H_2$ densities and the lowest temperature gas to trace the highest $H_2$ densities. This behavior results in the overprediction of the intensities of lowest-$N$ transitions and the underprediction of the intensities of the highest-$N$ transitions. This suggests that a single isobaric model to describe the $C_2H$ emitting gas is an oversimplification. In contrast, the PDR is known to be out of balance, showing signs of photoevaporation (Störzer & Hollenbach 1999). Figure 10 also shows that the $CH^+$ abundance peaks at lower visual extinctions than for $C_2H$ and is consistent with gas at higher temperatures and lower $H_2$ densities compared to $C_2H$, which was also confirmed by non-LTE radiative transfer models (Nagy et al. 2013). This

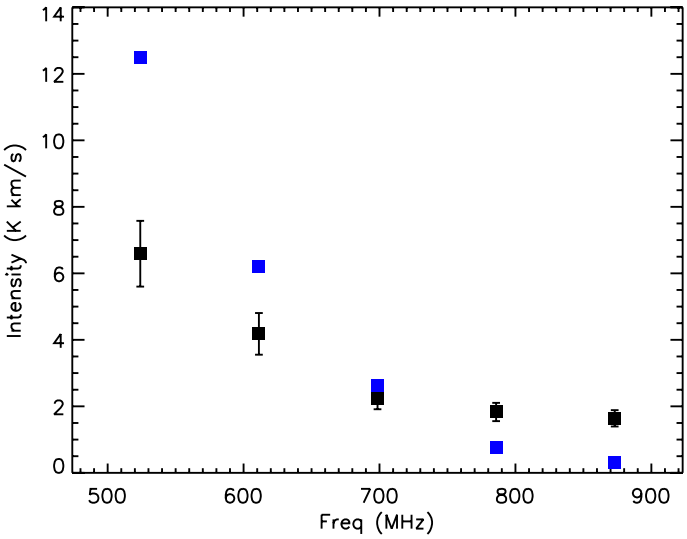


**Fig. 9.** $C_2H$ line intensity predictions from a PDR model with a pressure of $P = 10^8$ cm$^{-3}$ K and a radiation field of $\chi = 10^4$ (blue symbols) overplotted on the observations (black symbols).

supports the assumption that most $C_2H$ originates in a different gas compared to what $CH^+$ traces. The dominant $C_2H$ formation and destruction processes that the model suggests are shown in Sect. 7.

The PDR model quoted above is a simplification, but it confirms that $C_2H$ toward the Orion Bar originates in more than one pressure component. Based on the physical parameters suggested by the PDR model, the $C_2H$ emitting gas is also most likely to trace the edges of dense clumps exposed to UV irradiation close to the ionization front of the PDR. Moreover, $C_2H$ is predicted to be closely confined to the dense surface of the clump near $A_V \sim 1$. This is consistent with our excitation analysis, which argues that this gas is directly heated by the UV photons.

## 7. Formation and destruction processes

Even though we cannot constrain the formation and destruction of $C_2H$ with the observations presented in this paper, the PDR models explained above give an indication about the most important processes involved in the chemistry of $C_2H$. For Orion Bar conditions represented by the isobaric model with $P = 10^8$ K cm$^{-3}$ and $\chi = 10^4$, the most important processes that contribute in the formation of $C_2H$ are

$$H_2 + C_2 = C_2H + H \quad (2)$$
$$C_2H_2 + h\nu = C_2H + H \quad (3)$$
$$C_2H_2^+ + e^- = C_2H + H \quad (4)$$
$$C_3H^+ + e^- = C_2H + C. \quad (5)$$

These processes contribute ~67.1%, ~27.2%, ~4.8%, and ~0.9% of the total $C_2H$ abundance, respectively. These values refer to a depth equivalent to $A_V \sim 1$, which is part of the region, where $C_2H$ abundances peak. An alternative formation route of $C_2H$ can be expected in PDRs. Small hydrocarbons, such as $C_2H$, can form via the photodissociation of small PAHs ($N_C \leq 24$) (Useli Bacchitta & Joblin 2007). This formation route is not included in the Meudon PDR code, however, based on a comparison of the spatial distribution of $C_2H$ to that of a *Spitzer* map at 8 $\mu$m Cuadrado et al. (2015) conclude that this formation

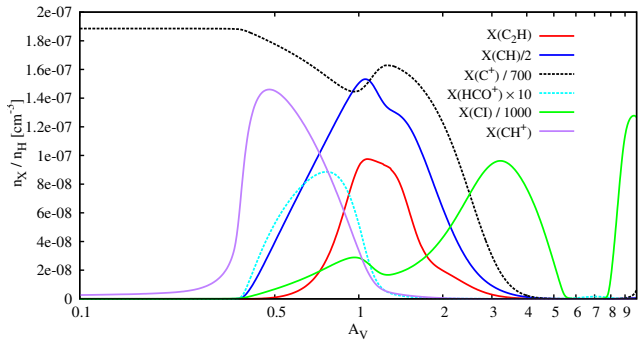


**Fig. 10.** Abundances of $C_2H$, CH, $C^+$, $HCO^+$, and [CI] corresponding to a PDR model with a pressure of $P = 10^8$ cm$^{-3}$ K, illuminated by a radiation field of $\chi = 10^4$ on the front, and a radiation field of $\chi = 10$ on the back side of the cloud.

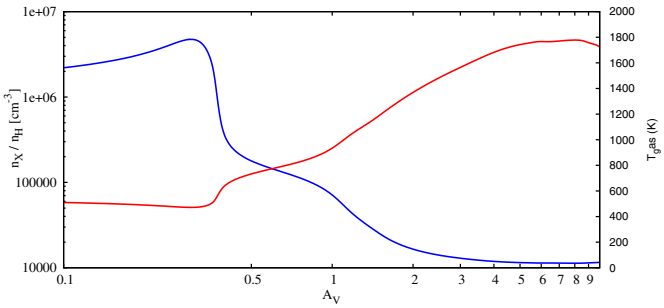


**Fig. 11.** Temperature (blue) and density (red) structure corresponding to the isobaric PDR model with a pressure of $P = 10^8$ cm$^{-3}$ K, illuminated by a radiation field of $\chi = 10^4$ on the front, and a radiation field of $\chi = 10$ on the back side of the cloud.

route cannot dominate the formation of $C_2H$ for the Orion Bar. The most important destruction processes at the same $A_V \sim 1$ are

$$C_2H + h\nu = H + C_2 \quad (6)$$
$$C_2H + H_2 = H + C_2H_2 \quad (7)$$
$$C_2H + C^+ = H + C_3^+. \quad (8)$$
$$C_2H + O \rightarrow CH + CO. \quad (9)$$

These processes are responsible for the destruction of ~68.1%, ~28.9%, ~1.5%, and 0.66% of $C_2H$, respectively. $C_2H$ abundances therefore peak in a region, where the molecular fraction ($f = 2N(H_2)/(N(H) + 2N(H_2))$) or $H_2$ density is high enough to produce $C_2H$ via reactions between $H_2$ and $C_2$, and the radiation field is low enough that the $C_2H$ production compensates for its destruction by FUV photons. With the used model parameters, the molecular fraction is 30%, the $H_2$ volume density about $10^5$ cm$^{-3}$, and the gas temperature is around 570 K at $A_V \sim 1$. At a depth equivalent to $A_V \sim 1.5$, where significant $C_2H$ is still located, the temperature decreases to about 270 K, the molecular fraction increases to ~50%, and the $H_2$ volume density is $3 \times 10^5$ cm$^{-3}$. The reaction rates are summarized in Table 2.

## 8. Discussion

We presented $C_2H$ observations toward the Orion Bar that correspond to five rotational transitions, in order to probe the physical parameters of the $C_2H$ emitting gas. The observed line intensities are not consistent with a single gas component, but suggest that $C_2H$ originates in at least two different components. The

**Table 2.** Rate coefficients for the formation and destruction reactions of $C_2H$ toward the Orion Bar.

| Reaction | $\alpha$ | $\beta$ | $\gamma$ | T (K) | Reference |
|---|---|---|---|---|---|
| (2) | $1.78 \times 10^{-10}$ | 0 | 1469 | 295–493 | Pitts et al. (1982) |
| (3) | $3.30 \times 10^{-9}$ | 0 | 2.27 | 10–41 000 | Van Dishoeck et al. (2006) |
| (4) | $1.35 \times 10^{-7}$ | −0.5 | 0 | – | Florescu-Mitchell & Mitchell (2006) |
| (5) | $1.50 \times 10^{-7}$ | −0.5 | 0 | 10–300 | Prasad & Huntress (1980) |
| (6) | $1.60 \times 10^{-9}$ | 0 | 2.3 | – | Van Hemert & Van Dishoeck (2008), Van Dishoeck et al. (2006) |
| (7) | $2.90 \times 10^{-12}$ | 1.75 | 539 | 178–4650 | Kruse & Roth (1997) |
| (8) | $1.00 \times 10^{-9}$ | −0.5 | 0 | 10–41000 | Prasad & Huntress (1980) |
| (9) | $1.00 \times 10^{-10}$ | 0.0 | 0 | 10–2500 | KIDA critical evaluation (based on experimental data) |

**Notes.** For two-body reactions, the rates are given by the Arrhenius-type formula of $\alpha\left(\frac{T}{300}\right)^{\beta}\exp\left(\frac{-\gamma}{T}\right)$ ($cm^3$ $s^{-1}$) and for photoreactions by the $k = \alpha\exp(-\gamma A_V)$ ($s^{-1}$) formula.

total $C_2H$ column density of about $10^{14}$ $cm^{-2}$ is dominated by gas corresponding to a kinetic temperature of 100 K to 150 K, which is consistent with the average value of 85 ± 30 K derived by Hogerheijde et al. (1995) and an $H_2$ volume density of $10^5$–$10^6$ $cm^{-3}$. The intensities of the higher-$N$ transitions suggest the existence of a higher density ($5 \times 10^6$ $cm^{-3}$) hot ($T \sim 400$ K) gas component. This high-pressure gas contributes only a small fraction of the $C_2H$ column density, but is required to explain the higher-$N$ $C_2H$ transitions. The rotational diagram is also consistent with at least two different gas components. A high-density gas component toward the Orion Bar, interpreted as photoevaporating dense clumps, was previously found to be traced by OH (Goicoechea et al. 2011). The rotational Λ-doublets detected using *Herschel*/PACS are consistent with warm (160–220 K) gas at densities of $n_H = 10^6$–$10^7$ $cm^{-3}$. The high-$N$ rotational transitions of $C_2H$ analyzed in this paper may trace similar areas of the dense filament surfaces.

Lower-$N$ $C_2H$ doublets ($N = 1$–$0, ..., 4$–$3$) toward the Orion Bar were analyzed by Cuadrado et al. (2015). Based on a rotational diagram analysis and assuming a uniform beam filling factor, they derived $C_2H$ column densities of $(4.2 \pm 0.2) \times 10^{14}$ $cm^{-2}$ and $(3.7 \pm 0.6) \times 10^{14}$ $cm^{-2}$ toward the dissociation front and the molecular peak of the Orion Bar, about a factor of four above the total $C_2H$ column density derived from the high-$N$ transitions presented in this paper. The rotational temperature they find for the $N = 1$–$0, ..., 4$–$3$ transitions is 26 ± 1 K, which is significantly below our cold-component temperature of 43 ± 0.2 K, determined from the $N = 6$–$5, ..., 8$–$7$ doublets. The combination of the higher column density and lower excitation temperature provides a similar flux around $N = 5$–$4$, which is consistent with our measurements, but leading to a continuation of our rotational diagram (Fig. 7) with a steeper slope towards lower energies. The low-$N$ observations of Cuadrado et al. (2015) therefore also trace somewhat more extended colder gas than our measurements. Based on non-LTE radiative transfer models, Cuadrado et al. (2015) estimate an $H_2$ volume density of $\gtrsim 10^5$ $cm^{-3}$ and a kinetic temperature of $\gtrsim$150 K. These parameters are close to those that our RADEX models suggest for the bulk of the $C_2H$ column density, corresponding mostly to the $N = 6$–$5, ..., 8$–$7$ doublets: $n(H_2) = 10^5$–$10^6$ $cm^{-3}$, $T_{kin} \sim 100$–$150$ K.

The $C_2H$ column density of $10^{14}$ $cm^{-2}$ can be converted to a $C_2H$ abundance using $C^{17}O$ transitions observed as part of our HIFI line survey (Nagy et al., in prep.). The beam-averaged $C^{17}O$ column density based on the four observed transitions (from 5–4 to 8–7) based on a rotational diagram is $1.3 \times 10^{15}$ $cm^{-2}$. This $C^{17}O$ column density is equivalent to a CO column density of $2.3 \times 10^{18}$ $cm^{-2}$, when adopting abundance ratios of $^{16}O/^{18}O = 560$ and $^{18}O/^{17}O = 3.2$ (Wilson & Rood 1994). Assuming a CO abundance of $1.1 \times 10^{-4}$ for the Orion Bar PDR (Johnstone et al. 2003), this CO column density is equivalent to an $H_2$ column density of $2.1 \times 10^{22}$ $cm^{-2}$. This value is close to the $N(H_2) = 3 \times 10^{22}$ $cm^{-2}$ derived by Cuadrado et al. (2015) close to the $CO^+$ peak position, based on the $C^{18}O$ 1–0, 2–1, and 3–2 transitions. This gives a $C_2H$ abundance of $5 \times 10^{-9}$ with respect to $H_2$. Van der Wiel et al. (2009) derived a $C_2H$ abundance of $2 \times 10^{-9}$ for a beam size of 15″. Fuente et al. (1996) derived a $C_2H$ abundance of $1.2 \times 10^{-8}$ with respect to $H_2$ toward the Orion Bar within a 26″ beam size. When deriving the $C_2H$ abundance with respect to the total hydrogen column density $N_H = N(H) + 2N(H_2)$, Cuadrado et al. (2015) measured $C_2H$ abundances of $(0.7$–$2.7) \times 10^{-8}$ with respect to H nuclei. Adding the $N(H) = 3 \times 10^{21}$ $cm^{-2}$ from Van der Werf et al. (2013) to our $H_2$ column, gives a $C_2H$ abundance of $2.2 \times 10^{-9}$ with respect to H nuclei. The higher $C_2H$ abundance measured by Cuadrado et al. (2015) is due to tracing a cooler component as well as using lower-$N$ transitions.

$C_2H$ has been detected toward other PDRs with various physical conditions, including Mon R2 (Rizzo et al. 2005; Ginard et al. 2012; Pilleri et al. 2013), the Horsehead PDR (Teyssier et al. 2004; Pety et al. 2005), and NGC 7023 (Fuente et al. 1993). Similar to what we found for the Orion Bar, multiple $C_2H$ transitions measured toward Mon R2 also suggest a two-component fit to describe $C_2H$ toward this region (Pilleri et al. 2013). However, only one of the two components found toward the Mon R2 region corresponds to a dense, highly UV-illuminated PDR, and the other to a low UV-illuminated lower density envelope. The PDR component toward Mon R2 originates in an $H_2$ volume density of $3 \times 10^6$ $cm^{-3}$, which is similar to what we found toward the Orion Bar for both components. Unlike the Orion Bar and Mon R2 PDRs, $C_2H$ toward the NGC 7023 region is likely to be related to a low-density envelope of NGC 7023, based on the comparison of the observations and chemical models (Fuente et al. 1993). $C_2H$ has also been detected toward the low UV-illumination (60 in Draine (1978) units) Horsehead PDR and was found to be spatially correlated with HCO (Gerin et al. 2009).

In addition to PDRs, $C_2H$ has also been detected in other types of regions. Watt et al. (1988) studied the $C_2H$ $N = 4$–$3$ transition in several molecular clouds. Based on the comparison of the observations and chemical models, they conclude that $C_2H$ emission arises from dense ($10^4$–$10^5$ $cm^{-3}$) gas, but not from very dense gas with $H_2$ densities of $>10^6$ $cm^{-3}$. Padovani et al. (2009) studied the $C_2H$ $N = 1$–$0$ and $N = 2$–$1$ transitions toward two prestellar cores and found evidence of deviations from LTE-level populations. Deviations from LTE are

also important in the case of the transitions studied here for the Orion Bar, since the excitation temperatures derived from the rotational diagrams are well below the kinetic temperatures derived using the non-LTE analysis. Beuther et al. (2008) studied $C_2H$ in regions that represent different evolutionary stages of high-mass star formation, including infrared dark clouds, high-mass protostellar objects, and ultracompact HII regions. Based on chemical models, they suggest that $C_2H$ traces the initial conditions of massive star formation. In the outer cloud regions discussed in their models, the $C_2H$ abundance is high because of the interstellar UV radiation field, which dissociates CO, enlarging the abundance of carbon. These outer cloud regions discussed by Beuther et al. (2008) also represent a similar case to PDRs, including the Orion Bar. Toward the DR21(OH) high-mass star-forming region, Mookerjea et al. (2012) found that the observed $C_2H$ and c-$C_3H_2$ abundances are consistent with a chemical model with an $H_2$ volume density of $5 \times 10^6$ cm$^{-3}$, similar to what our RADEX models suggest toward the Orion Bar. Apart from star-forming regions, $C_2H$ has also been detected toward several cold dark clouds (Wootten et al. 1980). These models explain that the $C_2H/HC_3N$ abundance ratio is consistent with gas-phase chemistry. $C_2H$ has been detected toward planetary nebulae including NGC 7027 (Zhang et al. 2008). Zhang et al. (2008) suggest that $C_2H$ is produced via the photodissociation of $C_2H_2$ toward this region. $C_2H$ has also been observed toward diffuse clouds (Lucas & Liszt 2000, Gerin et al. 2011). Both Lucas & Liszt (2000) and Gerin et al. (2011) suggest there is a correlation between $C_2H$ and c-$C_3H_2$ in diffuse clouds. Gerin et al. (2011) also suggest that $C_2H$ is a tracer of molecular hydrogen in diffuse and translucent gas.

Among the other environments mentioned above, $C_2H$ toward the Orion Bar is likely to trace a similar gas component to what was found toward Mon R2 and toward DR21(OH).

## 9. Conclusions

We have presented *Herschel*/HIFI observations of five high-$N$ $C_2H$ rotational doublets ($N = 6-5, ..., 10-9$) toward the $CO^+$ peak of the Orion Bar. These observations helped to constrain the excitation of $C_2H$. A single-component rotational diagram of $C_2H$ suggests a rotation temperature of 64 K and a $C_2H$ column density of $\sim 4 \times 10^{13}$ cm$^{-2}$. The rotational diagram is also consistent with two different gas components that correspond to rotation temperatures of 43 K and 123 K and to column densities of $8 \times 10^{13}$ cm$^{-2}$ and $2 \times 10^{13}$ cm$^{-2}$ for the three lower-$N$ and for the three higher-$N$ transitions, respectively.

A $C_2H$ $N = 6-5$ HIFI map shows $C_2H$ emission along the Orion Bar and perpendicular to it, corresponding to the Orion Ridge. Based on the comparison of the $C_2H$ integrated intensities to those of CH, $HCO^+$, and [CI], CH, and $HCO^+$ are the best $C_2H$ tracers both toward the Orion Ridge and toward the Orion Bar among the molecules studied in this paper. The calculated correlation coefficients toward the Orion Ridge (in the velocity interval of 7−8.5 km s$^{-1}$) are 0.92 and 0.89 for CH and $HCO^+$, respectively. The correlation coefficients toward redshifted velocities compared to the expected LSR velocity of the Orion Bar (10−11.5 km s$^{-1}$) are 0.88 and 0.89 for CH and $HCO^+$, respectively. The correlation between $C_2H$ and [CI] is lower toward both regions, suggesting that $C_2H$ and [CI] do not entirely trace the same gas.

Based on non-LTE radiative transfer models, the detected $C_2H$ line intensities are consistent with $C_2H$ to originate at least in two different gas components. One of these gas components dominates the $C_2H$ total column density and the intensity of the lower-$N$ transitions and can be related to warm ($T_{kin} \sim 100-150$ K) and dense ($n(H_2) \sim 10^5-10^6$ cm$^{-3}$) gas. The second component adds only a small fraction to the $C_2H$ column density, but is required to fit the intensity of the higher-$N$ transitions. This component is related to hot ($T_{kin} \sim 400$ K) and dense ($n(H_2) \sim 5 \times 10^6$ cm$^{-3}$) gas. A simple PDR model representing the Orion Bar with a plane-parallel slab of gas and dust confirms that $C_2H$ is likely to be related to more than a single pressure component, unlike $CH^+$ toward the Orion Bar.

Based on the physical parameters derived for the high-$N$ $C_2H$ transitions analyzed in this paper, the $N = 6-5, ..., 10-9$ $C_2H$ doublets may trace the edges of dense clumps exposed to UV radiation near the ionization front of the Orion Bar.

*Acknowledgements.* We thank the referee and the editor Malcolm Walmsley for useful comments that helped to improve our manuscript. We thank Robert Simon for providing us with a [CI] 1-0 NANTEN map. We also thank Franck Le Petit for discussions related to including the excitation of new species in the Meudon code. HIFI was designed and built by a consortium of institutes and university departments from across Europe, Canada, and the US under the leadership of SRON Netherlands Institute for Space Research, Groningen, The Netherlands, with major contributions from Germany, France, and the US. Consortium members are Canada: CSA, U.Waterloo; France: CESR, LAB, LERMA, IRAM; Germany: KOSMA,MPIfR,MPS; Ireland, NUIMaynooth; Italy: ASI, IFSI-INAF, Arcetri-INAF; Netherlands: SRON, TUD; Poland: CAMK, CBK; Spain: Observatorio Astronomico Nacional (IGN), Centro de Astrobiología (CSIC-INTA); Sweden: Chalmers University of Technology – MC2, RSS & GARD, Onsala Space Observatory, Swedish National Space Board, Stockholm University – Stockholm Observatory; Switzerland: ETH Zürich, FHNW; USA: Caltech, JPL, NHSC. HIPE is a joint development by the *Herschel* Science Ground Segment Consortium, consisting of ESA, the NASA Herschel Science Center, and the HIFI, PACS and SPIRE consortia.

## References

Andree-Labsch, S., Ossenkopf, V., & Röllig, M. 2014, A&A, submitted [arXiv:1405.5553]
Arab, H., Abergel, A., Habart, E., et al. 2012, A&A, 541, A19
Bergin, E. A., Phillips, T. G., Comito, C., et al. 2010, A&A, 521, L20
Beuther, H., Semenov, D., Henning, T., & Linz, H. 2008, ApJ, 675, L33
Bieging, J. H., Knee, L. B. G., Latter, W. B., & Olofsson, H. 1998, A&A, 339, 811
Cuadrado, S., Goicoechea, J. R., Pilleri, P., et al. 2015, A&A, 575, A82
de Jong, T., Dalgarno, A., & Chu, S.-I. 1975, ApJ, 199, 69
Draine, B. T. 1978, ApJS, 36, 595
Dubernet, M.-L., Alexander, M. H., Ba, Y. A., et al. 2013, A&A, 553, A50
Faure, A., & Lique, F. 2012, MNRAS, 425, 740
Florescu-Mitchell, A. I., & Mitchell, J. B. A. 2006, Phys. Rep., 430, 277
Flower, D. R. 2001, J. Phys. B, 34, 271
Fuente, A., Martín-Pintado, J., Cernicharo, J., & Bachiller, R. 1993, A&A, 276, 473
Fuente, A., Rodríguez-Franco, A., & Martín-Pintado, J. 1996, A&A, 312, 599
Gerin, M., Goicoechea1, J. R., Pety, J., & Hily-Blant, P. 2009, A&A, 494, 977
Gerin, M., Kaźmierczak, M., Jastrzebska, M., et al. 2011, A&A, 525, A116
Ginard, D., González-García, M., Fuente, A., et al. 2012, A&A, 543, A27
Goicoechea, J. R., Joblin, C., Contursi, A., et al. 2011, A&A, 530, L16
Harrison, S., & Tennyson, J. 2011, J. Phys. B: At. Mol. Opt. Phys., 44, 045206
Harrison, S., Faure, A., & Tennyson, J. 2013, MNRAS, 435, 3541
Hogerheijde, M. R., Jansen, D. J., & Van Dishoeck, E. F. 1995, A&A, 294, 792
Itikawa, Y., & Mason, N. 2005, Phys. Rep. 414, 1
Jansen, D. J., Spaans, M., Hogerheijde, M. R., & van Dishoeck, E. F. 1995, A&A, 303, 541
Johnstone, D., Boonman, A. M. S., & van Dishoeck, E. F. 2003, A&A, 412, 157
Kruse, T., & Roth P. 1997, J. Phys. Chem. A., 101, 2138
Le Petit, F., Nehmé, C., Le Bourlot, J., & Roueff, E. 2006, ApJS, 164, 506
Lis, D. C., & Schilke, P. 2003, ApJ, 597, 145
Lucas, R., & Liszt, H. S. 2000, 358, 1069
De Graauw, T., Helmich, F. P., Phillips, T. G., et al. 2010, A&A, 518, L6
Menten, K. M., Reid, M. J., Forbrich, J., & Brunthaler, A. 2007, A&A, 474, 515
Mookerjea, B., Hassel, G. E., Gerin, M., et al. 2012, A&A, 546, A75
Müller, H. S. P., Schlöder, F., Stutzki, J., & Winnewisser, G. 2005, J. Mol. Struct., 742, 215
Najar, F., Ben Abdallah, D., Spielfiedel, A., et al. 2014, Chem. Phys. Lett., 251
Nagy, Z., Van der Tak, F. F. S., Ossenkopf, V., et al. 2013, A&A, 550, A96

Neufeld, D. A. 2010, ApJ, 708, 635
Neufeld, D. A., Schilke, P., Menten, K. M., et al. 2006, A&A, 454, L37
Ott, S. 2010, in Astronomical Data Analysis Software and Systems XIX, eds. Y. Mizumoto, K.-I. Morita, & M. Ohishi, ASP Conf. Ser., 434, 139
Padovani, M., Walmsley, C. M., Tafalla, M., Galli, D., & Müller, H. S. P. 2009, A&A, 505, 1199
Pardo, J., Cernicharo, J., & Serabyn, E. 2001, IEEE Transactions on Antennas and Propagation, 49, 1683
Prasad, S. S., & Huntress, W. T. Tr. 1980, ApJS, 43, 1
Pety, J., Teyssier, D., Fossé, D., et al. 2005, A&A, 435, 885
Pety, J., Gratier, P., Guzmán, V., et al. 2012, A&A, 548, A68
Pilbratt, G. L., Riedinger, J. R., Passvogel, T., et al. 2010, A&A, 518, L1
Pilleri, P., Treviño-Morales, S., Fuente, A., et al. 2013, A&A, 554, A87
Pitts, W. M. L., Pasternack, L., & McDonald, J. R. 1982, Chem. Phys. 68, 417
Pratap, P., Dickens, J. E., Snell, R. L., et al. 1997, ApJ, 486, 862
Rizzo, J. R., Fuente, A., & García-Burillo, S. 2005, ApJ, 634, 1133
Simon, R., Stutzki, J., Sternberg, A., & Winnewisser, G. 1997, A&A, 327, 9
Schöier, F. L., van der Tak, F. F. S., van Dishoeck, E. F., & Black, J. H. 2005, A&A, 432, 369
Spielfiedel, A., Feautrier, N., Najar, F., et al. 2012, MNRAS, 421, 1891
Störzer, H., & Hollenbach, D. 1999, ApJ, 515, 669
Teyssier, D., Fossé, D., Gerin, M., et al. 2004, A&A, 417, 135
Tucker, K. D., Kutner, M. L., & Thaddeus, P. 1974, ApJ, 193, L115
Useli Bacchitta, F., & Joblin, C. 2007, in Molecules in Space and Laboratory, eds. P. J. L. Lemaire, & F. Combes (Publ. S. Diana), 89
Van der Tak, F. F. S., Black, J. H., Schöier, F. L., Jansen, D. J., & van Dishoeck, E. F. 2007, A&A, 468, 627
Van der Tak, F. F. S., Nagy, Z., Ossenkopf, V., et al. 2013, A&A, 560, A95
Van der Wiel, M. H. D., Van der Tak, F. F. S., Ossenkopf, V., et al 2009, A&A, 498, 161
van der Werf, P. P., Goss, W. M., & O'Dell, C. R. 2013, ApJ, 762, 101
Van Dishoeck, E. F., Jonkheid, B., van Hermaet, et al. 2006, Faraday Discussions, 133, 231
Van Hemert, M. C., & Van Dishoeck, E. F. 2008, Chem. Phys, 343, 292
Walmsley, C. M., Natta, A., Oliva, E., & Testi, L. 2000, A&A, 364, 301
Watt, G. D., White, G. J., Millar, T. J., & van Ardenne, A. 1988, A&A, 195, 257
Wilson, T. L., & Rood, R. 1994, ARA&A, 32, 191
Woon, D. E. 1995, Chem. Phys. Lett., 244, 45
Wootten, A., Bozyan, E. P., Garrett, D. B., Loren, R. B., Snell, R. L. 1980, ApJ, 239, 844
Zhang, Y., Kwok, S., & Dinh-V-Trung, 2008, ApJ, 678, 328

Pages 12 to 13 are available in the electronic edition of the journal at http://www.aanda.org

## Appendix A: $C_2H$–$e^-$ rate coefficients

The electronic ground-state symmetry of the radical $C_2H$ is $^2\Sigma^+$. Each rotational level $N$ is therefore split by the spin-rotation coupling between $N$ and the electronic spin $S = 1/2$ so that each rotational level $N$ has two sublevels given by $j = N \pm 1/2$. In addition, owing to the non-zero nuclear spin of the hydrogen atom ($I = 1/2$), each fine-structure level is further split into two hyperfine levels $F = j \pm 1/2$. The rotational constant of $C_2H$ is 1.46 cm$^{-1}$. The fine- and hyperfine-splittings are typically 0.01 and 0.001 cm$^{-1}$, respectively. The dipole moment of $C_2H$ is 0.77 D (Woon 1995).

There is, to our knowledge, no previous estimate for the electron-impact hyperfine excitation rate coefficients of the $C_2H$ radical. Recent R-matrix calculations have considered electron scattering from $C_2H$ (Harrison & Tennyson 2011), but they concentrated on bound states of the anion and electronic excitation of the neutral. Here, electron-impact hyperfine rate coefficients for $C_2H$ were computed using a three-step procedure, similar to the one employed recently for the radicals $OH^+$ (Van der Tak et al. 2013) and CN (Harrison et al. 2013): i) rotational excitation rate coefficients for the dipolar ($\Delta N = 1$) transitions were first computed using the Born approximation; ii) fine-structure excitation rate coefficients were then obtained from the Born rotational rates using the (scaled) infinite-order sudden (IOS) approximation; and iii) hyperfine excitation rate coefficients were finally obtained again using the IOS approximation. In the case of polar molecules, the long-range electron dipole interaction is well known to control the rotational excitation, especially at low collision energies (Itikawa & Mason 2005). Although the $C_2H$ dipole is only moderate, the Born approximation is expected to be reasonably accurate for dipolar transitions. In practice, Born cross-sections were computed for collision energies ranging from 1 meV to 1 eV, and rate coefficients were deduced for temperatures from 10 K to 1000 K. The IOS approximation was employed to derive the fine-structure rate coefficients in terms of the rotational rates for excitation out of the lowest rotational level $N = 0$, following the general procedure of Faure & Lique (2012) (see Eqs. (1)–(3) of Harrison et al. 2013). The IOS approximation was also applied to derive the hyperfine rate coefficients (Eqs. (6)–(8) in Harrison et al. 2013).

The above three-step procedure was applied to the first 26 rotational levels of $C_2H$, which is up to the level $(N, j, F) = (25, 24.5, 24)$, which lies 945 cm$^{-1}$ above the ground state (0, 0.5, 0), resulting in 246 collisional transitions. The largest rate coefficients are on the order of $5 \times 10^{-7}$ cm$^3$ s$^{-1}$, i.e. typically four orders of magnitude more than the $C_2H$-He rate coefficients, and they are expected to be accurate to within a factor of 2. The complete set of de-excitation rate coefficients is available online from the LAMDA (Schöier et al. 2005) and BASECOL (Dubernet et al. 2013) databases.

## Appendix B: Extrapolation of collision rates

Spielfiedel et al. (2012) only provided collision rates for temperatures up to 100 K and for rotational levels with up to $N = 8$ corresponding to an upper level energy of about 150 K, as given in BASECOL. This is clearly insufficient for modeling our observations because we observed up to $N = 10$–9, the gas temperatures in the Orion Bar are around 150 K, and densities of more than $10^6$ cm$^{-3}$ allow for a collisional excitation of much higher levels that will eventually decay radiatively, feeding the rotational ladder from levels above $N = 9$. A solution of the rate equations for the Orion Bar conditions thus asks for the inclusion of levels with energies of a few times the kinetic temperature.

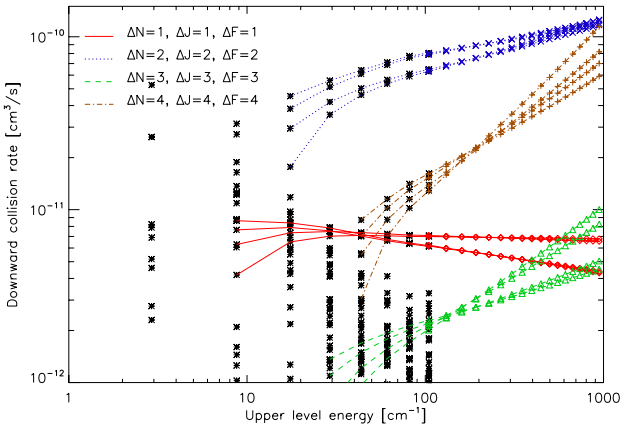


**Fig. B.1.** Rates for the de-excitation of $C_2H$ through collision with $H_2$ at 100 K. Black crosses mark all collision rates from Spielfiedel et al. (2012) above $10^{-12}$ cm$^3$s$^{-1}$. The curves indicate the different transition series for pure rotational transitions of the molecule, i.e., $\Delta N = \Delta J = \Delta F$. Each series consists of four curves according to the fine and hyperfine structure split of the four $N$ states with approximately the same energy: $J = N \pm /1/2$ and $F = J \pm 1/2$. The continuations of those curves into the colored symbols show the extrapolation of the rates to the higher level transitions using the formalism from Schöier et al. (2005) based on the IOS approximation.

Thus we have to extrapolate the rate coefficients from Spielfiedel et al. (2012) in terms of both additional levels and higher temperatures. A very general, but numerically demanding approach to extrapolating collision rates was proposed by Neufeld (2010). It is applicable to any type of molecule, but needs some "training" through collision rates from similar species. For $C_2H$ we have, however, the advantage that it is basically a linear rotor, only superimposed by the hyperfine interaction. Since our measurements show no variation in the hyperfine ratio, and the collision rates from Spielfiedel et al. (2012) at temperatures above 20 K are dominated by the pure rotational transitions of the linear configuration with $\Delta N = \Delta J = \Delta F$ (see Fig. B.1), it seems justified to concentrate on the rates for these transitions and to treat $C_2H$ as a simple linear rotor.

For such molecules, the IOS approximation is a handy approach to computing the collision rates for any series of $\Delta J$ (see Appendix A) as long as the energy difference of the states is small compared to the kinetic energy of the collision partners. For higher levels, a correction is possible, as summarized by Schöier et al. (2005). We use here their Eq. (13) derived originally by de Jong et al. (1975), Bieging et al. (1998) to extrapolate the collision coefficients to higher levels based on the energy-level difference and the behavior of the collision rates for lower $J$ levels in the series. Owing to the additional hyperfine split in $C_2H$, we have to perform the fit individually for the different $F - J$ combinations in a pure rotational series. This assumes that we have no further interaction of the states, as justified by the behavior of the collision rates at temperatures between 20 K and 100 K. The result is shown in Fig. B.1. This figure shows the collision-rate behavior within the dominant series for the levels computed by Spielfiedel et al. (2012) and the extrapolation of the rates up to $N = 18$. All other collision rates are much lower so that they are not important for the population of the upper levels.

Besides the extrapolation to higher level energies, we also need to extrapolate the rates from Spielfiedel et al. (2012) to

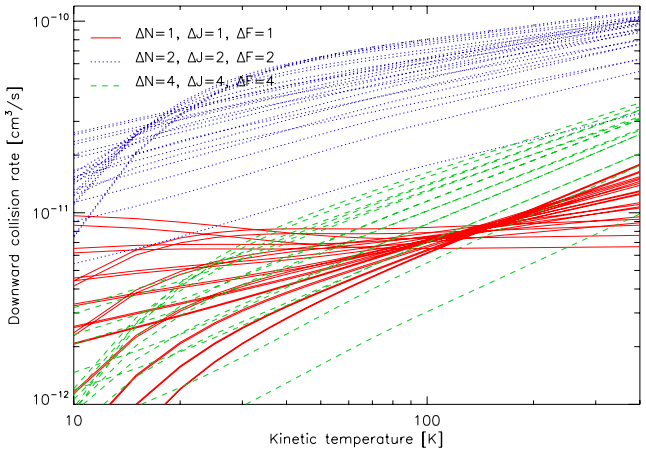


**Fig. B.2.** Temperature dependence for the main collision rates of $C_2H$ with $H_2$. The curves are sorted by $\Delta J$ but cover all transitions of the corresponding series. Every connected dot in Fig. B.1 produces one temperature-dependence graph in this plot. To improve the readability, we have omitted the $\Delta N = \Delta J = \Delta F = 3$ series here. Up to 100 K, the lines show the rates computed by Spielfiedel et al. (2012), from 100 to 400 K, and we extrapolated as a power law with the same slope as measured between 90 and 100 K.

higher temperatures. To obtain the rate at higher temperatures, we have to compute the integral over collision cross sections for energies of about ten times the kinetic temperature of the gas (Flower 2001). This makes the high-temperature computations demanding, in principle. However, since we only want to expand the temperature range by a small extent, from 100 K to 400 K, we can use the temperature behavior measured up to 100 K to estimate the rates above this temperature. The simplest approach would be an extrapolation with the square root of temperature, reflecting the velocity of the collision partners. When inspecting the rate coefficients at temperatures up to 100 K, we see, however, that the majority of the rates show a temperature dependence that is very different from an exponent of 0.5 (see Fig. B.2). But the double-logarithmic plot shows straight lines for basically all rate coefficients at high temperatures, indicating that a power-law extrapolation with a free exponent is a good description of the temperature dependence. The curvature in the curves is very small.

We extrapolated from 100 K to 400 K using the power law determined either between 80 K and 100 K or between 90 K and 100 K. When comparing the two extrapolations, we found only 11 transitions with a deviation of about 10%. All other transitions showed better agreement of the rates, proving that the power-law description is quite accurate. One should take into account, however, that this approach should not be continued over wide dynamic ranges because we clearly expect the coupling to change when dealing with factors of ten or more.

To check the sensitivity of our overall results to the extrapolations, we also ran the RADEX fits performed in Sect. 5 with an alternative collision rate file created just by a constant continuation of the rates from 100 K toward higher temperatures and higher levels. For the same input parameters, the average excitation temperature then drops from 26.9 K to 24.6 K, eventually indicating an overall relatively minor sensitivity of our results to the details of the extrapolations.

We finally note that rate coefficients for the fine-structure excitation of $C_2H$ by para-$H_2(j = 0)$ have been published recently by Najar et al. (2014). The largest rate coefficients, which correspond to transitions with $\Delta j = \Delta N = 2$, were found to differ from those of $C_2H$-He by a factor of ~1.4, as assumed here. Larger differences were, however, observed for other transitions, especially those with $\Delta j = \Delta N = 1$ (see Fig. 6 in Najar et al. 2014). Hyperfine-resolved rate coefficients for $C_2H$-$H_2$, for high levels and high temperatures, are therefore urgently required in order to avoid both collider-mass scaling and extrapolations.